

Double Hopf bifurcation in corotating spiral Poiseuille flow

Marc Avila,^{a)} Alvaro Meseguer,^{b)} and Francisco Marques^{c)}

Departament de Física Aplicada, Univ. Politècnica de Catalunya, C/ Jordi Girona 1-3, Mod. B5, 08034 Barcelona, Spain

(Received 17 January 2006; accepted 10 April 2006; published online 1 June 2006)

Nonlinear dynamics of the spiral Poiseuille problem for moderate axial through flow is investigated numerically within the corotating regime for medium gap geometry. The neighborhood of a double Hopf bifurcation point of the linear stability boundary, where spiral waves of opposite axial phase propagation compete, is explored by accurately solving time-dependent Navier-Stokes equations with a solenoidal spectral method. The mode interaction generates a quasiperiodic stable regime of interpenetrating spirals, which coexists with stable limit cycles associated with the aforementioned spiral waves of opposite helicoidal orientation. The spatiotemporal properties of the computed solutions are explained and discussed in terms of equivariant bifurcation and normal form theories. Similar flows have also been observed experimentally in the past within the corotating region.

© 2006 American Institute of Physics. [DOI: 10.1063/1.2204967]

I. INTRODUCTION

The spiral Poiseuille problem deals with the behavior of an incompressible viscous fluid confined between two coaxial cylinders independently rotating around their common axis. In addition, the fluid is enforced to flow downstream by an imposed pressure gradient in the axial direction. The resulting steady spiral flow is a combination of a rotation due to the azimuthal Couette flow and an axial parabolic profile, due to the pressure gradient, also termed *spiral Poiseuille flow*¹ (SPF). The SPF is subject to *shear* and *centrifugal* instability mechanisms, which can destabilize the flow for sufficiently high values of the axial pressure gradient and angular speeds of the cylinders. The nonlinear study of the complex secondary flows arising in terms of symmetry breaking bifurcations constitutes a major challenge.

The stability of this flow was studied experimentally by Snyder² for narrow gap geometry and a fixed outer cylinder, showing that the primary transition leads to axially propagating structures. For low values of the through flow, the transition is observed to toroidal vortices, which are superseded by spiral vortices for higher values of the through flow.^{2,3} A most interesting feature of this flow was reported by Nagib,⁴ who observed secondary flows where two spiral structures coexist simultaneously in space and time in the corotating regime. The systematic exploration of secondary flows for this problem has also been studied more recently for a fixed outer cylinder,^{5,6} who observed several flow regimes of toroidal and spiral vortices. The velocity fields of some of these regimes were carefully studied⁷ and compared to their counterparts in the case of no axial flow, i.e., Taylor–Couette.

A saddle-point analysis⁸ of the counter-rotating SPF has recently provided the boundaries between convective and absolute instabilities for low through flow, the results being confirmed experimentally.⁹ Recent numerical computations¹⁰

based on a hybrid finite-differences-Galerkin method have also studied nonlinear dynamics of the SPF for moderate axial flow, also focusing on the counter-rotating regime.

Former numerical linear stability analyses of the SPF were carried out in the axisymmetric case^{11,12} or for specific angular rotation speed ratio values of the cylinders.^{3,13} A first comprehensive linear stability analysis^{14,15} for medium gap geometry covered a wide range of independent corotating angular speeds of the cylinders as well as axial flow velocities, where a bicritical curve of the coexistence of spiral waves of opposite helical orientation was provided. Over that curve, two, or even three, independent modes bifurcate simultaneously. Linear stability analysis cannot predict which of these secondary regimes will be dominant beyond transition, and a nonlinear analysis is required.

In this work we study the nonlinear dynamics of the SPF within the *corotating* regime and for moderate axial flow speed. In particular, we focus on the competition between spiral waves of opposite axial phase velocity and azimuthal wavenumbers, $n = \pm 1$, in the neighborhood of a double Hopf point. Our approach combines the general theory of double Hopf bifurcations with nonlinear spectrally resolved computations, allowing the identification of the scenario corresponding to the present case. Assuming axial periodicity, the incompressible Navier-Stokes equations, along with the axisymmetric nonslip boundary conditions on the inner and outer cylinders, are invariant to rotations around the common axis of the cylinders and also to axial translations, endowing the system with the $SO(2) \times SO(2)$ symmetry group. These symmetries play a key role in the spatiotemporal properties of the secondary regimes and also their stability, as predicted by equivariant bifurcation and normal form theories.

Experimental explorations of the corotating SPF carried out by Nagib in the 1970s for a small gap revealed the presence of secondary stable regimes consisting of a superposition of traveling spiral waves of opposite helicoidal orientation.⁴ As noted by Joseph, these flows are characterized by traveling spirals with very high axial and azimuthal

^{a)}Electronic mail: marc@fa.upc.edu

^{b)}Electronic mail: alvar@fa.upc.edu

^{c)}Electronic mail: marques@fa.upc.edu

wavenumbers, thus being unfeasible to reproduce them numerically, due to the current computational limitations.¹ The results obtained in the present study provide numerical evidence of the existence of these secondary regimes for much lower angular and streamwise speeds of the flow, where the spatial resolution required is less demanding.

The paper is structured as follows. The mathematical and numerical formulation of the problem are presented in Sec. II. Section III is devoted to a general description of the double Hopf bifurcation scenario corresponding to the case of study. The main results are presented in Sec. IV, where different secondary regimes are studied in a neighborhood of the bicritical point. In Appendix A we address specific technical details regarding the numerical method. Finally, the normal form associated with the double Hopf bifurcation with the $SO(2) \times SO(2)$ symmetry group is obtained in Appendix B, where the spatiotemporal properties of the bifurcated solutions are discussed within the framework of the dynamical systems theory.

II. FORMULATION AND NUMERICAL METHOD

We consider an incompressible fluid of kinematic viscosity ν and density ϱ that is contained between two concentric rotating cylinders whose inner and outer radii and angular velocities are r_i^* , r_o^* , and Ω_i , Ω_o , respectively. In addition, the fluid is driven by an imposed axial pressure gradient. The independent dimensionless parameters appearing in this problem are the radius ratio $\eta = r_i^*/r_o^*$, which fixes the geometry of the annulus; the Couette flow Reynolds numbers, $Ri = dr_i^* \Omega_i / \nu$ and $Ro = dr_o^* \Omega_o / \nu$ of the rotating cylinders, where $d = r_o^* - r_i^*$ is the gap between the cylinders, and the axial Reynolds number, $Re = \bar{w}d / \nu$, where \bar{w} is the mean axial flow velocity in the annulus, and measures the imposed axial pressure gradient.

Henceforth, all variables will be rendered dimensionless using d , d^2 / ν , and ν^2 / d^2 as units for space, time, and the reduced pressure ($p = p^* / \varrho$), respectively. The Navier-Stokes equation and the incompressibility condition for this scaling become

$$\partial_t \mathbf{v} + (\mathbf{v} \cdot \nabla) \mathbf{v} = -\nabla p + \Delta \mathbf{v}, \quad \nabla \cdot \mathbf{v} = 0. \quad (1)$$

Let $\mathbf{v} = (u, v, w)$ be the physical components of the velocity field in cylindrical coordinates (r, θ, z) . The boundary conditions for \mathbf{v} are

$$v(r_i) = Ri, \quad v(r_o) = Ro, \quad (2)$$

where $r_i = r_i^* / d = \eta / (1 - \eta)$, $r_o = r_o^* / d = 1 / (1 - \eta)$ are the nondimensional radii of the cylinders. The steady velocity field \mathbf{v}_B (spiral Poiseuille flow), independent of the axial and azimuthal coordinates (θ, z) , and satisfying (1) and (2) is

$$\begin{aligned} \mathbf{v}_B &= (u_B, v_B, w_B) \\ &= [0, C_1 r + C_2 / r, C_3 \ln(r/r_o) + C_4(r^2 - r_o^2)], \end{aligned} \quad (3)$$

where

$$C_1 = (Ro - \eta Ri) / (1 + \eta), \quad (4)$$

$$C_2 = \eta(Ri - \eta Ro) / [(1 - \eta)(1 - \eta^2)], \quad (5)$$

$$C_3 = -2(1 - \eta^2) \text{Re} / [1 - \eta^2 + (1 + \eta^2) \ln \eta], \quad (6)$$

$$C_4 = (1 - \eta)(\ln \eta) C_3 / (1 + \eta). \quad (7)$$

Throughout the paper we will use (Ri, Ro) as nondimensional parameters, keeping $\eta = 0.5$ and $\text{Re} = 33$ fixed. In addition, we assume that the flow is L^* periodic in the axial direction. In cylindrical nondimensional coordinates (r, θ, z) , the spatial domain of the problem is $\mathcal{D} = [r_i, r_o] \times [0, 2\pi] \times [0, \Lambda]$, where $\Lambda = L^* / d$ is the aspect ratio.

The governing equations are invariant to rotations R_α about the cylinder axis and to axial translations T_a :

$$R_\alpha(\mathbf{v})(r, \theta, z) = \mathbf{v}(r, \theta + \alpha, z), \quad (8)$$

$$T_a(\mathbf{v})(r, \theta, z) = \mathbf{v}(r, \theta, z + a). \quad (9)$$

Rotations generate the symmetry group $SO(2)$, and due to the imposed axial periodicity, axial translations generate another $SO(2)$ symmetry group. As rotations and translations commute, the complete symmetry group of the problem is $\mathcal{G} = SO(2) \times SO(2)$. The steady basic flow (3) is invariant to \mathcal{G} .

The velocity field consists of the basic velocity field \mathbf{v}_B and pressure p_B , and perturbations \mathbf{u} , q :

$$\mathbf{v}(r, \theta, z, t) = \mathbf{v}_B(r) + \mathbf{u}(r, \theta, z, t), \quad (10)$$

$$\nabla \cdot \mathbf{u} = 0, \quad \mathbf{u}(r = r_i) = \mathbf{u}(r = r_o) = \mathbf{0}, \quad (11)$$

$$p(r, \theta, z, t) = p_B(z) + q(r, \theta, z, t). \quad (12)$$

\mathbf{u} is a solenoidal velocity field vanishing at the cylinder walls. This decomposition simplifies the numerical scheme. On introducing the perturbed fields in the Navier-Stokes equations, we obtain a nonlinear initial-boundary problem for the perturbations \mathbf{u} and q :

$$\partial_t \mathbf{u} = -\nabla q + \Delta \mathbf{u} - (\mathbf{v}_B \cdot \nabla) \mathbf{u} - (\mathbf{u} \cdot \nabla) \mathbf{v}_B - (\mathbf{u} \cdot \nabla) \mathbf{u}, \quad (13)$$

$$\nabla \cdot \mathbf{u} = 0, \quad (14)$$

$$\mathbf{u}(r_i, \theta, z, t) = \mathbf{u}(r_o, \theta, z, t) = \mathbf{0}, \quad (15)$$

$$\mathbf{u}(r, \theta + 2\pi, z, t) = \mathbf{u}(r, \theta, z, t), \quad (16)$$

$$\mathbf{u}(r, \theta, z + \Lambda, t) = \mathbf{u}(r, \theta, z, t), \quad (17)$$

$$\mathbf{u}(r, \theta, z, 0) = \mathbf{u}_0, \quad \nabla \cdot \mathbf{u}_0 = 0, \quad (18)$$

for $(r, \theta, z) \in \mathcal{D}$ and $t > 0$. Equation (13) describes the nonlinear space-time evolution of the perturbation of the velocity field. Equation (14) is the solenoidal condition for the perturbation, and Eqs. (15)–(17) describe the homogeneous boundary conditions for the radial coordinate and the periodic boundary conditions for the azimuthal and axial coordinates, respectively. Finally, Eq. (18) is the initial solenoidal condition for the perturbation field at $t = 0$.

We discretize the perturbation \mathbf{u} by a solenoidal spectral approximation \mathbf{u}_s of order L in z , order N in θ , and order M in r ,

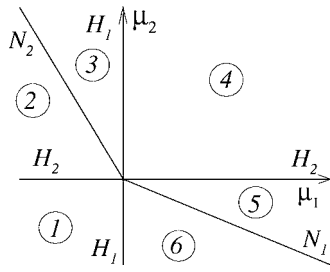


FIG. 1. Parametric portrait for a simple type IV double Hopf bifurcation. The curves H_1 and H_2 (coinciding with the axes $\mu_1=0$ and $\mu_2=0$, respectively), are the two Hopf bifurcation curves at which the limit cycles, P_1 and P_2 , bifurcate supercritically from the basic state P_0 . The curves N_1 and N_2 are Neimark-Sacker bifurcation curves at which the quasiperiodic mixed mode P_3 bifurcates. Phase portraits in each of the six regions indicated are shown in Fig. 2.

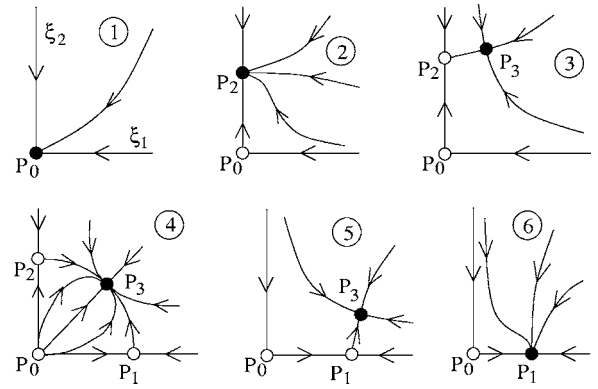


FIG. 2. Generic phase portraits corresponding to the six different regions of the double Hopf bifurcation of type IV simple in Fig. 1. Solid (open) circles are stable (unstable) states. ξ_1, ξ_2 are proportional to the amplitudes squared: $\xi_1 = -p_{11}r_1^2, \xi_2 = -p_{22}r_2^2$; see Appendix B for details.

$$\mathbf{u}_S(r, \theta, z, t) = \sum_{l=-L}^L \sum_{n=-N}^N \sum_{m=0}^M a_{lmn}(t) \Phi_{lmn}(r, \theta, z), \quad (19)$$

where Φ_{lmn} are *trial* bases of solenoidal vector fields of the form

$$\Phi_{lmn}(r, \theta, z) = e^{i(lk_0 z + n\theta)} \mathbf{v}_{lmn}(r), \quad (20)$$

with $k_0 = 2\pi/\Lambda$, satisfying

$$\nabla \cdot \Phi_{lmn} = 0 \quad (21)$$

for $(l, n, m) \in [-L, L] \times [-N, N] \times [0, M]$. The trial bases (20) are therefore $(\Lambda, 2\pi)$ periodic in the axial and azimuthal directions, respectively. The radial functions \mathbf{v}_{lmn} appearing in (20) must satisfy homogeneous boundary conditions at the inner and outer radii of the cylinders,

$$\mathbf{v}_{lmn}(r_i, \theta, z) = \mathbf{v}_{lmn}(r_o, \theta, z) = \mathbf{0}. \quad (22)$$

The spectral scheme is accomplished when introducing expansion (19) in (13) and projecting over a suitable set of *test* solenoidal fields,

$$\Psi_{lmn} = e^{i(lk_0 z + n\theta)} \tilde{\mathbf{v}}_{lmn}. \quad (23)$$

Both sets \mathbf{v}_{lmn} and $\tilde{\mathbf{v}}_{lmn}$ can be found in the Appendix A. The projection is carried out via the standard volume integral over the domain \mathcal{D} ,

$$(\Psi_{lmn}, \partial_t \mathbf{u}_S)_{\mathcal{D}} = (\Psi_{lmn}, \Delta \mathbf{u}_S - (\mathbf{v}_B \cdot \nabla) \mathbf{u}_S - (\mathbf{u}_S \cdot \nabla) \mathbf{v}_B - (\mathbf{u}_S \cdot \nabla) \mathbf{u}_S)_{\mathcal{D}}, \quad (24)$$

for $(l, n, m) \in [-L, L] \times [-N, N] \times [0, M]$, where

$$(\mathbf{a}, \mathbf{b})_{\mathcal{D}} = \int_{\mathcal{D}} \mathbf{a}^* \cdot \mathbf{b} \, d\mathcal{D}, \quad (25)$$

and where $*$ stands for the complex conjugate. The pressure term is canceled in the projection,¹⁶ i.e., $(\Psi_{lmn}, \nabla q)_{\mathcal{D}} = 0$, leading to a dynamical system only involving the amplitudes $a_{lmn}(t)$ of the velocity approximation (19), i.e.,

$$A_{pqr}^{lmn} \frac{da_{pqr}}{dt} = B_{pqr}^{lmn} a_{pqr} - N_{lmn}(a, a), \quad (26)$$

where we have used the convention of summation with respect to repeated subscripts. In (26), the matrices \mathbf{A} and \mathbf{B} stand for the projection of the time differentiation and linear Laplacian-advection operators, whereas \mathbf{N} is the projected nonlinear advective term. The system of ODE's (26) is integrated in time by means of a linearly implicit method, where backward differences are used for the linear part and polynomial extrapolation is used for the nonlinear one. Overall, the solenoidal scheme used here is mainly based on previous spectral schemes recently formulated and extensively tested for cylindrical geometries.^{17,18} Nevertheless, the spectral accuracy of the scheme and the convergence of the time stepper have been tested and compared with linear and nonlinear former spectral Galerkin computations of flows in annular geometries.^{15,19}

III. $SO(2) \times SO(2)$ -DOUBLE HOPF BIFURCATION: TRANSITION SCENARIOS

In the double Hopf bifurcation, the presence of $SO(2) \times SO(2)$ symmetry alters the generic normal form only in the presence of resonances. In Appendix B, we present a derivation of the normal form for the double Hopf bifurcation with $SO(2) \times SO(2)$ symmetry. We show that the symmetries inhibit resonances, as in the double Hopf bifurcation with $SO(2)$ symmetry²⁰ and with $SO(2) \times Z_2$ symmetry.²¹ The resonance condition is, in this instance, $\omega_2^0/\omega_1^0 = n_2/n_1 = k_2/k_1$; ω_i^0 are the Hopf frequencies at the bifurcation, n_i are the critical azimuthal wavenumbers, and k_i are the critical axial wavenumbers. Resonance is only possible if the frequencies and the azimuthal and axial wavenumbers are in the same ratio. We shall show below that our double Hopf bifurcation is not resonant, so its corresponding normal form is that for the generic double Hopf bifurcation. In terms of the moduli and phases of the complex amplitudes of the eigenvectors, the normal form can be written, up to fourth order, as (B19),

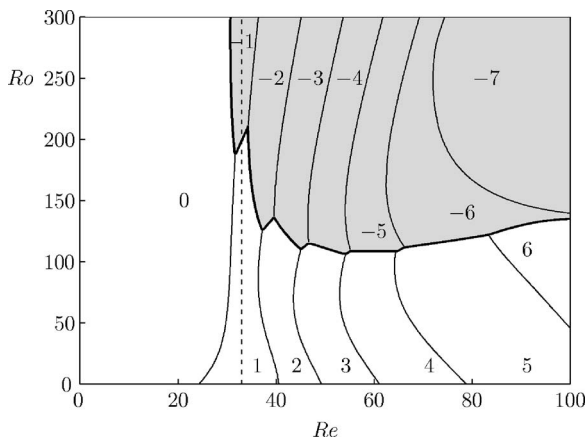


FIG. 3. Projection of the critical surface $Ri^c(Re, Ro)$ on the (Re, Ro) plane, following Meseguer and Marques (Ref. 15.) Boundary curves separate regions where modes of different azimuthal wavenumber n (included in the plot) bifurcate at the lowest Ri . The bold line represents the bicritical boundary crossed by the dashed line at $Re=33$.

$$\begin{aligned}
 \dot{r}_1 &= r_1(\mu_1 + p_{11}r_1^2 + p_{12}r_2^2 + q_1r_2^4), \\
 \dot{r}_2 &= r_2(\mu_2 + p_{21}r_1^2 + p_{22}r_2^2 + q_2r_1^4), \\
 \dot{\phi}_1 &= \omega_1^0 + \psi_1(r_1, r_2, \mu_1, \mu_2), \\
 \dot{\phi}_2 &= \omega_2^0 + \psi_2(r_1, r_2, \mu_1, \mu_2),
 \end{aligned}
 \tag{27}$$

where μ_1 and μ_2 are the normalized bifurcation parameters and $\mu_1 = \mu_2 = 0$ at the bifurcation point. An expression for $\mu_{1,2}$ is given in Sec. IV as a function of the physical parameters for the actual problem. The p_{ij} , and q_i depend on the parameters μ_1 and μ_2 , and satisfy a nondegeneracy condition in the neighborhood of the bifurcation, $p_{ij} \neq 0$.

The normal form (27) admits a multitude of distinct dynamical behaviors, depending on the values of p_{ij} and q_i . These are divided into so-called *simple* ($p_{11}p_{22} > 0$) and *difficult* ($p_{11}p_{22} < 0$) cases. In the simple cases, the topology of the bifurcation diagram is independent of the q_i terms. Even in the simple case, several different bifurcation diagrams exist. A comprehensive description of all the simple and difficult scenarios is given in Ref. 22. In our problem, the double Hopf bifurcation is of simple type IV, as rendered by computations presented in Sec. IV. The remainder of this section is devoted to a qualitative description of this scenario.

Figure 1 shows the parametric portrait in a neighborhood of the double Hopf bifurcation point, for the case corresponding to our problem. Parameter space is divided into six regions, delimited by bifurcation curves. The number of solutions and their stability is different in each region. Figure 2 shows typical phase portraits in these six different regions. P_1 and P_2 are spiral waves with negative and positive azimuthal wavenumbers emerging from the basic state P_0 when the Hopf bifurcation curves H_1 and H_2 are crossed. There is a region (3, 4, and 5 in Fig. 1) where a stable two-torus solution P_3 (interpenetrating spirals of opposite azimuthal wavenumber) exists. In this scenario, there is precisely one stable solution in each of the six regions in parameter space.

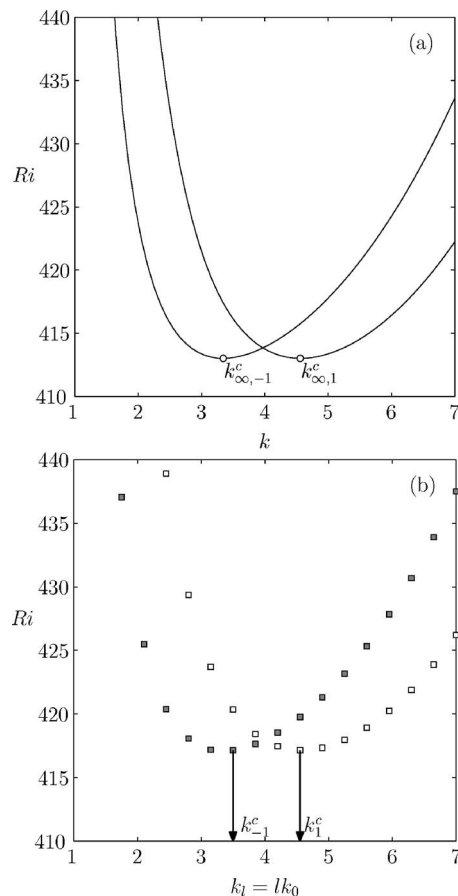


FIG. 4. (a) Neutral stability curves for $n = \pm 1$ azimuthal modes at the bicritical point $(Re, Ro) = (33, 200.48)$, for k varying continuously; the white circles are located at the minima $k_{\infty,-1}^c$ and $k_{\infty,1}^c$ of $n = -1$ and $n = 1$, respectively. (b) The same as (a), evaluated at the bicritical point $(Re, Ro) = (33, 206)$, for the particular discretization $k = lk_0$, $l \in [-66, 66]$.

IV. RESULTS

A comprehensive linear stability analysis of the steady SPF has recently been carried out for medium gap geometry,^{14,15} covering a wide range of independent corotating angular speeds Ri, Ro of the cylinders and axial flow velocities Re , providing a bicritical curve where spiral patterns featuring opposite axial propagation compete. Figure 3 shows a projection of the critical surface $Ri = Ri^c(Re, Ro)$, as computed in former linear stability analyses,¹⁵ where the aforementioned bicritical curve (bold line) is shown. In the gray region, above the bicritical curve, upstream propagating spiral waves are dominant, whereas below that curve the spiral waves propagate downstream, i.e., with the imposed axial flow. Downstream (upstream) propagation of the spiral patterns corresponds to positive (negative) azimuthal wavenumbers of the bifurcating modes.

In this work we present a study of the nonlinear dynamics arising in the neighborhood of a double Hopf point of the aforementioned bicritical curve. For computational reasons, the bicritical point at $Re=33$ (the dashed line in Fig. 3) has been chosen, since the bifurcated spirals feature the lowest nonzero azimuthal wavenumbers $n = \pm 1$.

Figure 4(a) shows the neutral stability curves (k, Ri^c) provided by the linear stability analysis for $Re=33$ and

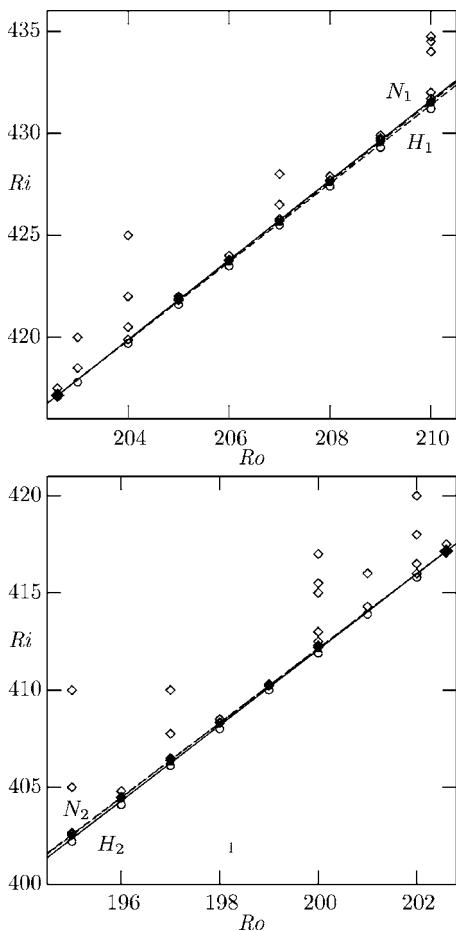


FIG. 5. Loci of the solution type in (Ro, Ri) space; \circ are steady SPF, \blacksquare are L-SW, \bullet are R-SW, and \diamond are IPS. The double Hopf point (29) is located at \blacklozenge .

$Ro=200.48$. The curves associated with the azimuthal modes $n=1$ and $n=-1$ attain a common minimum Reynolds number $Ri=413.02$ at $k_{\infty,1}^c=4.56$ and $k_{\infty,-1}^c=3.343$, respectively; the ∞ subindex refers to critical values computed assuming a continuous range of axial wavenumbers k . The location of the corresponding bicritical point is

$$(Re, Ro, Ri)_{\infty}^{dH} = (33, 200.48, 413.02). \tag{28}$$

When considering nonlinear computations, the spectrum of axial wavenumbers becomes discrete (20), and it has to be suitably fixed so that the discretization resolves those modes responsible for the instability, as well as their harmonics. At this point, a fundamental axial wavenumber has to be fixed so that the aforementioned discretization covers the unstable dynamics. Therefore, a good choice for k_0 appearing in (20) is crucial to reproduce the critical axial wavenumbers found in the infinite cylinder case where the axial wavenumber k is continuous.

In the present work we use a spectral resolution consisting of $(L, M, N)=(66, 24, 8)$ modes along with $k_0=0.35$, leading to an aspect ratio $\Lambda \sim 18$. The value of k_0 has been suitably chosen in order to capture the two values $k_{\infty,1}^c$ and $k_{\infty,-1}^c$. This is accomplished by the axial discretization used, where the modes $(l, n)=(13, 1)$ and $(l, n)=(10, -1)$ consistently reproduce the nearby critical $k_1^c=13k_0=4.55$ and $k_{-1}^c=10k_0=3.5$ values of the continuum case, respectively. In

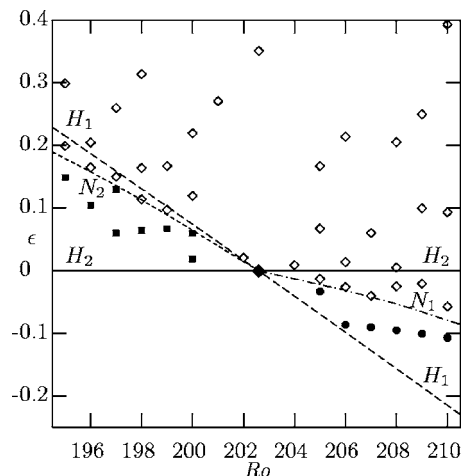


FIG. 6. Loci of the solution type in (Ro, ϵ) space ($\epsilon=Ri-Ri_2^c$); \blacksquare are L-SW, \bullet are R-SW, and \diamond are IPS. The double Hopf point (29) is located at \blacklozenge .

addition, up to four harmonics of the two previous modes are also included in the dynamical system of amplitudes. Nevertheless, the resulting equispaced set of discretized axial wavenumbers lk_0 leads to minor discrepancies when trying to reproduce the instability mechanisms. This is mainly due to the fact that the critical Reynolds number Ro at which these modes bifurcate simultaneously is slightly different from the ideal value $Ro_{\infty}=200.48$. This small discrepancy can be spotted from Fig. 4(b), where the neutral stability points $(lk_0, Ri^c)_{n=\pm 1}$ attain a common critical value $Ri^c=417.15$ for $Ro=202.6$. As a result, the coordinates of the double Hopf bifurcation point based on our discretization are

$$(Re, Ro, Ri)_{\text{discrete}}^{dH} = (33, 202.6, 417.15). \tag{29}$$

Overall, the critical values of the spectral approximation differ nearly by 1% from the values obtained by linear stability computations using a continuous range of k .

The linear stability of the basic flow (3) has been studied in region

$$\mathfrak{R} = \{Re = 33, (Ro, Ri) \in [190, 210] \times [390, 435]\}, \tag{30}$$

for the spectral discretization above. The Hopf bifurcation curves $Ri_1^c=H_1(Ro)$ and $Ri_2^c=H_2(Ro)$ in \mathfrak{R} were computed, rendering the double Hopf point $H_1 \cap H_2$ (29). In this particular case, the expressions for the normalized bifurcation parameters $\mu_{1,2}$ appearing in (27), are

$$\mu_1 = Ri - (1.949Ro + 22.05), \tag{31}$$

$$\mu_2 = Ri - (1.952Ro + 21.75), \tag{32}$$

where $H_i=\{\mu_i=0\}$, for $i=1, 2$. The Neimark-Sacker bifurcation curves N_1 and N_2 in Fig. 1 have been computed by time evolution, using the three dimensional (3D) Navier-Stokes solver. Figure 5 shows the bifurcation curves and the computed solutions indicating their nature. The four bifurcation curves $H_1, H_2, N_1,$ and N_2 in Fig. 5 are very close together. For clarity, in Fig. 6 these curves are represented in (Ro, ϵ) space, where $\epsilon=Ri-H_2(Ro)$, allowing us to distinguish the

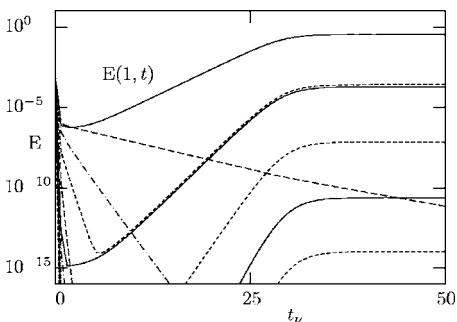


FIG. 7. Time evolution of the energy of the azimuthal Fourier modes, measured according to (33), during the transition from SPF to L-SW at $(Ro, Ri)=(190, 392.85)$. The solid upper line corresponds to the $n=1$ mode generating L-SW whereas the stagnated curves below $E(1, t)$ correspond to harmonics of the leading unstable mode.

six regions of the corresponding theoretical scenario in Fig. 1.

The steady spiral Poiseuille flow SPF is stable below H_1 and H_2 curves. The stability of any solution is monitored in time through the measurement of the kinetic energy density associated with each azimuthal Fourier mode

$$E(n, t) = \frac{1}{2V} \int_0^\Lambda dz \int_0^{2\pi} d\theta \int_{r_i}^{r_o} \mathbf{u}_n^* \cdot \mathbf{u}_n r dr, \quad (33)$$

where V is the volume of the cylinder and \mathbf{u}_n is the n azimuthal component of the perturbation field.

$$\mathbf{u}_n(r, z, t) = \sum_{l=-L}^L \sum_{m=0}^M a_{lmn}(t) e^{i(lk_0 z + n\theta)} \mathbf{v}_{lmn}(r). \quad (34)$$

When crossing H_2 from below, the basic flow becomes unstable, as shown in the energy-time plot of Fig. 7. The instability leads to a secondary regime consisting of a stable limit cycle corresponding to spiral vortices of azimuthal wavenumber $n=1$ rotating and propagating in the axial direction, henceforth termed as *Left spiral waves* (L-SW).

In order to detect the Neimark-Sacker boundary N_2 , the L-SW was continued by increasing Ri until the limit cycle eventually became unstable, as shown in its energy-time evolution; see Fig. 8. In this case, the instability leads to a stable quasiperiodic mixed mode consisting of *Interpenetrating spirals* (IPS).

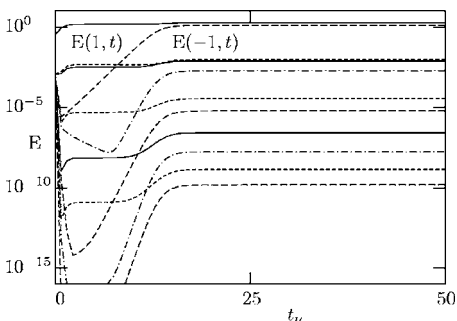


FIG. 8. The same as Fig. 7 during the transition from L-SW to IPS at $(Ro, Ri)=(190, 393.5)$. The solid (dashed) upper line corresponds to the $n=1$ ($n=-1$) mode.

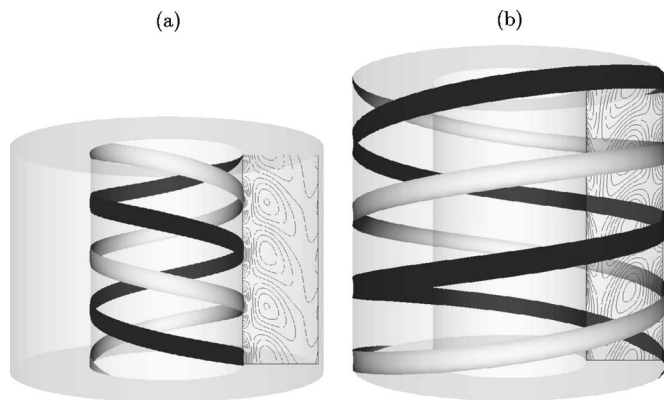


FIG. 9. Isosurfaces of the azimuthal vorticity of the perturbation: (a) L-SW at $(Ro, Ri)=(190, 392.85)$, $\omega_\theta = \pm 23$. (b) R-SW at $(Ro, Ri)=(210, 431.5)$, $\omega_\theta = \pm 9.5$.

The same scenario was observed when crossing H_1 from below, leading to a stable limit cycle between H_1 and N_1 that corresponds to propagating spiral vortices of opposite azimuthal wavenumber $n=-1$, i.e., *Right spiral waves* (R-SW). As shown in Fig. 5, the regions where L-SW or R-SW are stable are very narrow, whereas the mixed mode solution is stable in a much wider region of parameter space. Note that the stability region for the L-SW is slightly wider than the R-SW, Figure 6. In addition, all the bifurcations observed were found to be supercritical.

A. Characterization of L-SW and R-SW solutions

The spiral patterns arising from Hopf bifurcations H_1 (R-SW) and H_2 (L-SW) break the rotational and translational symmetries of the problem. However, these solutions are time-periodic and, essentially, one-dimensional, since their dependence on t, z and θ occurs through the *phase variable*¹⁰

$$\phi = \omega t + lk_0 z + n\theta. \quad (35)$$

Therefore, these patterns rotate with angular speed $w_p = -\omega/n$ and propagate axially with phase speed $c = -\omega/(lk_0)$, so that the symmetries have become spatiotemporal, see Appendix B Eqs. (B26) and (B27). These solutions retain a purely spatial symmetry, a combination of an axial translation T_a and a rotation R_α such that

TABLE I. Angular and axial speeds of L-SW and R-SW measured at points located within the boundaries H_1 - N_1 and H_2 - N_2 of Fig. 5. The axial speed c of the patterns has been normalized with respect to the Reynolds number Re .

L-SW	Ro	Ri	ω_p	c/Re	R-SW	Ro	Ri	ω_p	c/Re
	195	402.5	397.7	2.65		205	421.8	27.53	-0.24
	196	404.4	398.9	2.66		206	423.7	28.24	-0.24
	197	406.3	400.0	2.66		207	425.65	28.99	-0.25
	198	408.25	401.2	2.67		208	427.6	29.72	-0.26
	199	410.2	402.4	2.68		209	429.55	30.45	-0.26
	200	412.1	403.5	2.69		210	431.5	31.19	-0.27

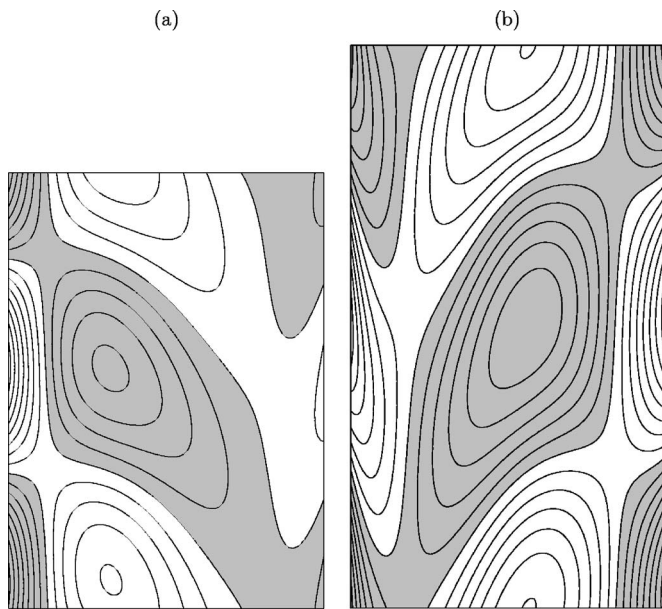


FIG. 10. Contours of the azimuthal vorticity of the perturbation $(\nabla \times \mathbf{u})_\theta$ evaluated over a θ -constant cross section for $(r, z) \in [r_i, r_o] \times [0, h_{L,R}]$. (a) L-SW at $(R_o, R_i)=(190, 392.85)$; (b) R-SW at $(R_o, R_i)=(210, 431.5)$. For clarity, the original aspect ratio has been preserved in the plots.

$$lk_0 z + n\theta = 0, \tag{36}$$

corresponding to helical motion. Therefore the symmetry $H_\alpha = R_\alpha T_{-n\alpha/(lk_0)}$ generates a subgroup $SO(2)_H$ of \mathcal{G} , see Appendix B for details. These spiral patterns are simultaneously rotating and traveling waves, resembling a barber pole, and for this reason we use the term *spiral waves* for them. The geometrical shape of these solutions can be seen in Fig. 9, showing isosurfaces of azimuthal vorticity. Each spiral wave

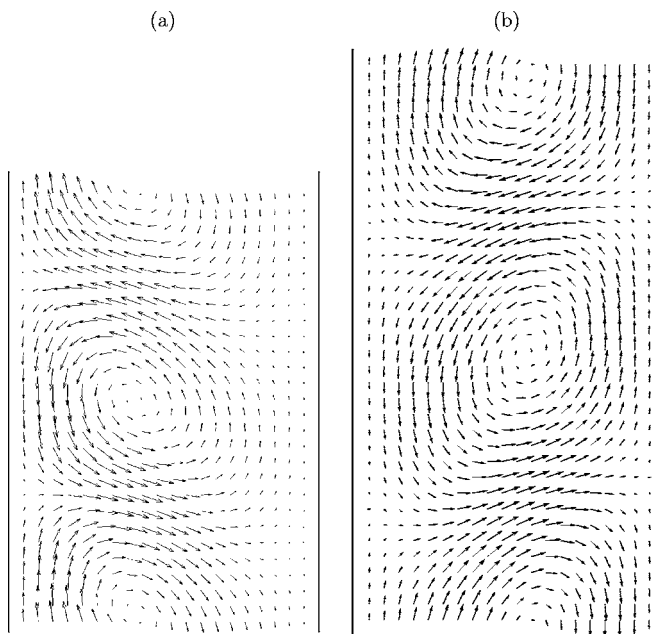


FIG. 11. Perturbation vector field components (u_r, u_z) evaluated over a θ -constant cross section for $(r, z) \in [r_i, r_o] \times [0, h_{L,R}]$. (a) L-SW at $(R_o, R_i)=(190, 392.85)$, (b) R-SW at $(R_o, R_i)=(210, 431.5)$. For clarity, the original aspect ratio has been preserved in the plots.

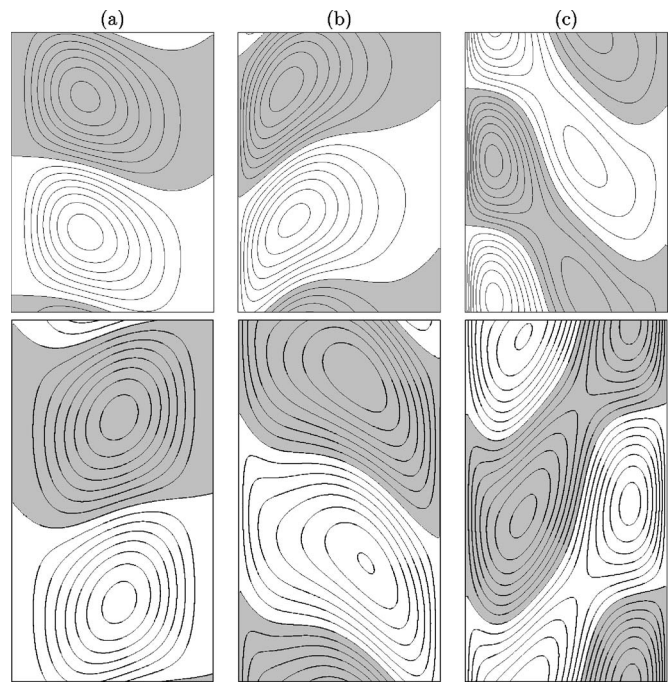


FIG. 12. Contours of the perturbation field \mathbf{u} evaluated over a θ -constant cross section for $(r, z) \in [r_i, r_o] \times [0, h_{L,R}]$. Top, L-SW at $(R_o, R_i)=(190, 392.85)$ and bottom, (R-SW) at $(R_o, R_i)=(210, 431.5)$. From left to right: (a) u_r , (b) u_θ ; and (c) u_z components. Gray and white regions stand for negative and positive or zero values, respectively.

is composed of two spiral vortices with opposite vorticity (light and dark in the figure), within an axial wavelength.

Within the explored regions between H_1-N_1 and H_2-N_2 , the R-SW and L-SW are found to corotate with the cylinders, precessing with angular speeds of order $\omega_p^L \sim 400$ and $\omega_p^R \sim 30$, respectively. However, the L-SW pattern exhibits a downstream phase speed c faster than the base flow axial mean velocity (measured by Re), whereas the R-SW slowly propagate upstream. It is shown in the Appendix B that opposite axial propagation is a sufficient condition to inhibit resonances, thus the case of study is nonresonant. Accurate angular and axial speeds of these described patterns within their domains of stability are reported in Table I.

The L-SW have an axial wavelength of $h_L=1.38$ and are mainly concentrated on the inner cylinder wall, where strong azimuthal vorticity spots are generated, as shown in Fig. 10(a). On the other hand, the R-SW have an axial wavelength of $h_R=1.8$ but are mainly concentrated on the outer cylinder wall, where similar azimuthal vorticity spots are produced, as shown in Fig. 10(b). However, for the L-SW the azimuthal vorticity is confined within a region close to the inner cylinder, whereas the R-SW feature high values of the azimuthal vorticity along all the radial domain. Figure 11 shows the perturbation velocity field \mathbf{u} on a θ -constant cross section, for both solutions in Fig. 10. The center of the vortices is slightly displaced toward the inner (outer) cylinder for the L-SW (R-SW). Figure 12 shows contours of the components of the perturbation velocity \mathbf{u} for both solutions. Their maxima and minima are also located near the inner (L-SW) or outer (R-SW) cylinders, as occurs with the azimuthal vorticity.

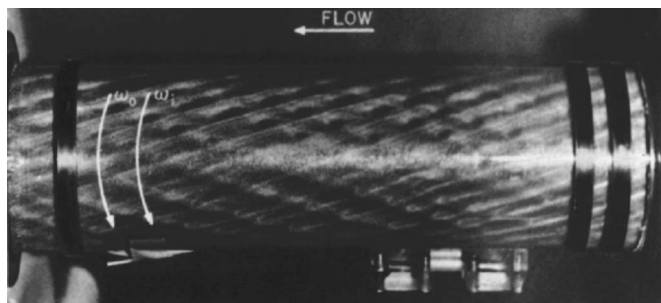


FIG. 13. DSSF experimental flow found by Nagib (Ref. 4) for $Re=120$, $Ro=898$, $Ri=835$, and for small gap geometry with $\eta=0.77$.

B. Characterization of IPS solutions

The interpenetrating spirals (IPS) consist of quasiperiodic regimes exhibiting the main features of the two limit cycles corresponding to L-SW and R-SW. Similar interpenetrating spirals regimes were found experimentally in the past by Nagib,⁴ termed as *Double Spiral Secondary Flow* (DSSF). The experiments were carried out at higher Reynolds numbers Re , Ro , Ri than our computations, and with a smaller gap $\eta=0.77$. Figure 13 shows a photograph of the aforementioned DSSF found by Nagib.⁴ Recent linear stability results²³ suggest that these solutions come from a similar instability mechanism, although much higher azimuthal modes (typically within the range $13 \leq |n| \leq 15$) are responsible for the transition, rendering nonlinear computations unaffordable.

The dependence of the IPS on t , z , and θ occurs through the two independent phase variables,

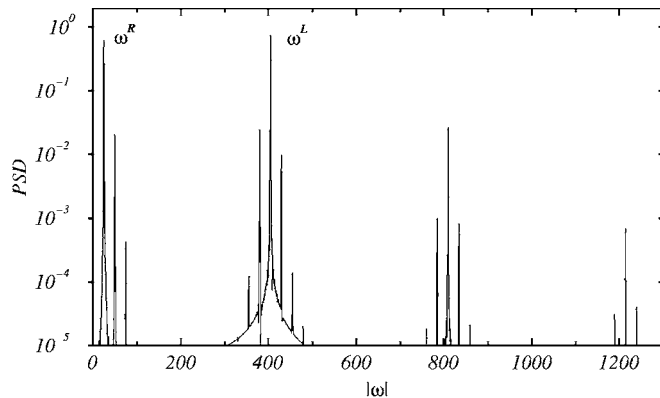
$$\phi^L = \omega^L t + k^L z + \theta, \tag{37}$$

$$\phi^R = \omega^R t + k^R z - \theta, \tag{38}$$

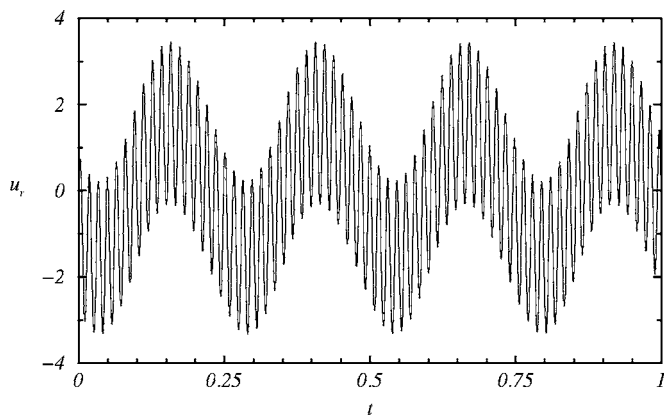
corresponding to the unstable L-SW and R-SW. This fact, predicted in Appendix B using normal form theory, is confirmed by the good agreement between the frequencies observed in the IPS regime and the eigenfunctions of the linear stability problem that generate L-SW and R-SW (disagreement below a 0.5%). The power spectral density of the IPS is plotted in Fig. 14(a), where the associated L-SW and R-SW frequencies and their harmonics are clearly observed. The two frequencies differ in more than one order of magnitude, being ω^R about 16 times smaller than ω^L . They can be clearly observed in the time series of the radial velocity at a convenient point, shown in Fig. 14(b).

The IPS regime can be interpreted as a superposition of two waves, with phases ϕ^L and ϕ^R , corresponding to L-SW and R-SW, respectively, but precessing with different angular speeds while propagating downstream and upstream, respectively. Angular and axial speeds of both waves are also provided in Table II. Figure 15 shows isosurfaces of the azimuthal vorticity and helicity of the perturbation velocity field \mathbf{u} , illustrating that the waves associated with the L-SW and R-SW are clustered on the inner and outer cylinder, respectively.

In order to illustrate the opposite axial propagation of the L-SW and R-SW components of the interpenetrating spirals



(a)



(b)

FIG. 14. (a) Power spectral density of the IPS solution at $(Ro, Ri) = (201, 414.3)$. The two independent frequencies are very close to the frequencies of the unstable R-SW ($\omega^R=24.82$) and L-SW ($\omega^L=-404.6$) solutions, respectively. (b) Time series of u_r for the IPS solution in (a).

IPS, several snapshots of the azimuthal vorticity at different times are shown in Fig. 16, where the two periods $T^L=2\pi/\omega^L \approx 0.016$ and $T^R=2\pi/\omega^R \approx 0.25$ have been considered. In the first row, covering one T^L period, we observe the downstream propagation associated with the L-SW, clearly concentrated on the inner cylinder. In the second row, covering one T^R period, the upstream propagation associated with the R-SW is observed on the outer cylinder (note that downstream propagation corresponds to motion on the positive axial direction in the plots). The interaction of the two spiral waves, R-SW and L-SW, with different periods and axial wavelengths, makes it difficult to analyze the resultant pat-

TABLE II. Angular and axial speeds of the IPS measured at some points located over N_1 and N_2 curves of Fig. 5.

IPS	Ro	Ri	ω_p^L	c^L/Re	ω_p^R	c^R/Re
	195	402.65	397.7	2.65	20.42	-0.18
	198	408.5	401.2	2.67	22.62	-0.20
	201	414.3	404.6	2.69	24.82	-0.21
	204	422	408.7	2.72	28.27	-0.24
	207	426.5	411.9	2.74	29.53	-0.26
	210	432	415.3	2.77	31.73	-0.27

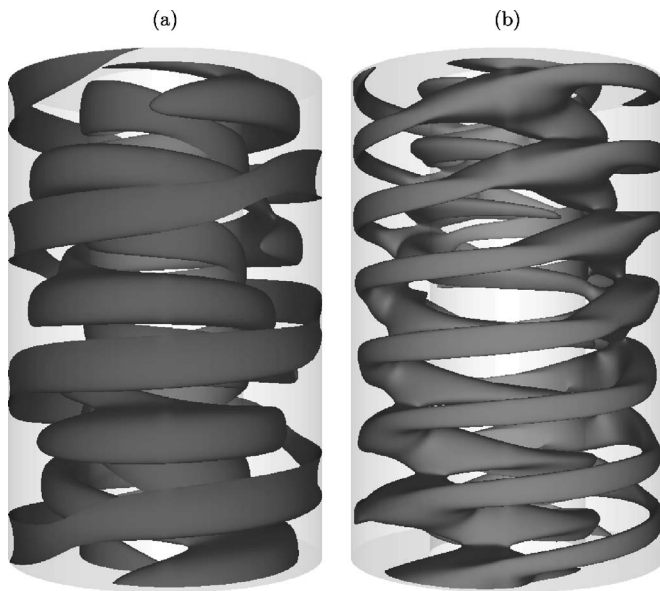


FIG. 15. Isosurfaces of the IPS solution at $(Ro, Ri) = (201, 414.3)$, $z \in [0, \Lambda/3]$. (a) Azimuthal vorticity of the perturbation at level $\omega_\theta = -10$. (b) Helicity of the perturbation $H = \mathbf{u} \cdot (\nabla \times \mathbf{u})$ at level $H = 0.2$.

tern, except where one of the spiral waves is clearly dominant, i.e., close to the inner or the outer cylinder.

The interpenetrating spirals IPS are quasiperiodic both in space and time. Quasiperiodicity in time is clearly manifested in Fig. 14(b). Figure 17 shows the vector field \mathbf{u} and contours of its components on a θ -constant section for the IPS regime. The radial-azimuthal velocity field clearly shows a nonuniform cell height throughout the cross section, as a result of the incommensurate wavelengths of the R-SW and L-SW spiral waves. The superposition of the two coexisting solutions is better seen in the azimuthal velocity contours (the third column of Fig. 17), where a Λ shape is identified close to the mean radius. The axial wavelengths corresponding to the L-SW (R-SW) can still be identified close to the inner (outer) cylinder in the contours for u_r (compare with Fig. 12).

V. CONCLUSIONS

Nonlinear dynamics of the corotating spiral Poiseuille flow with constant through flow have been investigated numerically by means of an accurate solenoidal spectral method that solves the time-dependent three-dimensional Navier-Stokes equations assuming axially periodic boundary conditions.

The explorations have been focused on a neighborhood of a double Hopf point where low azimuthal modes compete. Normal form analysis with the symmetry group $\mathcal{G} = SO(2) \times SO(2)$ has been combined with a numerical exploration for different inner/outer cylinder velocities, allowing the identification of the bifurcation scenario corresponding to this problem. It has been shown that the symmetry group \mathcal{G} does not alter the generic normal form but imposes a stronger constraint for resonance, rendering the present case of study non-resonant.

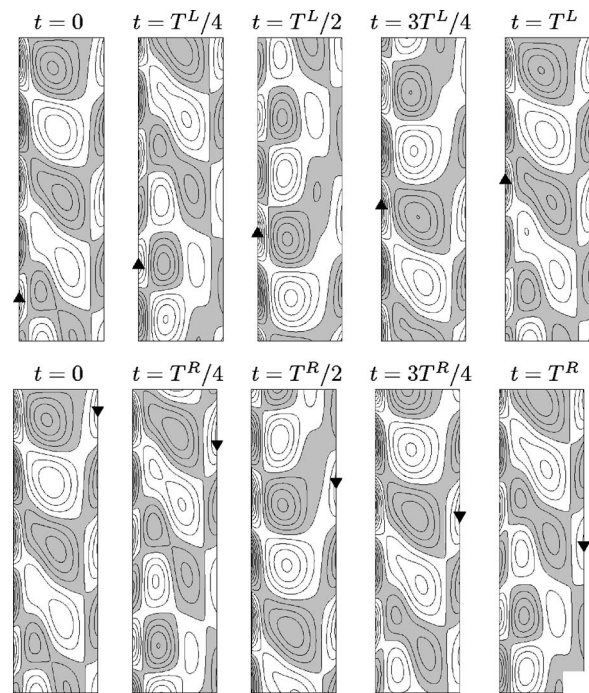


FIG. 16. Contours of the azimuthal vorticity of the perturbation, $(\nabla \times \mathbf{u})_\theta$, for the IPS at $(Ro, Ri) = (201, 414.3)$ evaluated over a θ -constant cross section for $(r, z) \in [r_i, r_o] \times [0, 2h_R]$. The first (second) row illustrates the upward (downward) propagation associated to the L-SW (R-SW), indicated with \blacktriangle (\blacktriangledown).

Numerical simulations confirm that spiral vortices of opposite wavenumber $n = \pm 1$ and a mixed mode solution of interpenetrating spirals are born at the double Hopf bifurcation. All these solutions break both $SO(2)$ symmetries, though in the case of the spiral waves L-SW and R-SW the symmetries become spatiotemporal.

In the present study, the dominant solution is the quasiperiodic state IPS, which is stable in a wide region of parameter space, confining the spiral waves periodic solutions L-SW and R-SW to a very narrow parameter region. L-SW and R-SW can be viewed as rotating and traveling waves that precess with independent angular speeds, corotating with the cylinders, but exhibit opposite streamwise phase propagation. The stability region for the downstream traveling L-SW is slightly wider than the upstream R-SW, as observed in the counter-rotating case.¹⁰ The stable IPS solution can be regarded as the superposition of both pure mode solutions, where the features of the L-SW and R-SW regimes can be observed close to the inner and outer cylinder, respectively, where one or the other are dominant. The spatiotemporal properties of the computed solutions are in very good agreement with bifurcation theory predictions provided.

The coexistence of spiral patterns of opposite helical orientation and streamwise propagation had been formerly observed experimentally in this problem for much higher angular speeds of the cylinders and also for narrow gap geometries, where the dominant azimuthal modes at transition are one order of magnitude larger than in the present study, thus being extremely expensive a well-resolved computation of the resulting patterns with current computational capabilities.

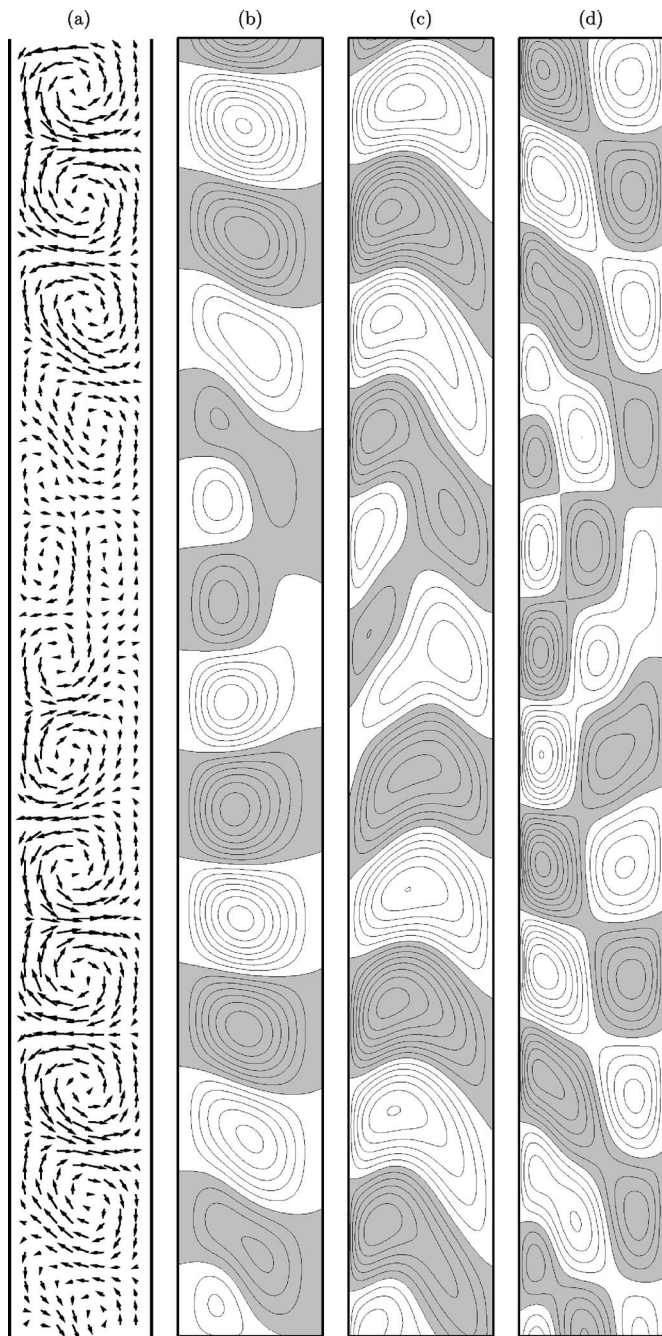


FIG. 17. Perturbation vector field \mathbf{u} corresponding to the IPS solution at $(Ro, Ri) = (201, 414.3)$ evaluated on a θ -constant cross section for $(r, z) \in [r_i, r_o] \times [0, \Lambda/2]$. (a) Vector field (u_r, u_z) , (b) contours of u_r , (c) contours of u_θ , and (d) contours of u_z .

Above the studied range of inner and outer angular speeds, additional bifurcations take place, and the dynamics may exhibit more complex mode interactions. These issues will be addressed in future works.

ACKNOWLEDGMENTS

This work was supported by the Spanish Government Grants No. FIS2004-01336 and No. AP-2004-2235, and by the Catalan Government Grant No. SGR-00024.

APPENDIX A: SOLENOIDAL SPECTRAL BASES

In what follows, we define

$$\delta = \frac{1 + \eta}{1 - \eta}, \quad x(r) = 2r - \delta, \quad (\text{A1})$$

that maps the radial domain $r \in [r_i, r_o]$ to the interval $x \in [-1, 1]$, and

$$h_m(r) = (1 - x^2)T_m(x), \quad g_m(r) = (1 - x^2)^2T_m(x), \quad (\text{A2})$$

where $T_m(r)$ is the Chebyshev polynomial of degree m , and $w(x) = 1/\sqrt{1-x^2}$ is the weight function within the interval $(-1, 1)$. The functions in (A2) satisfy

$$h_m(r_i) = h_m(r_o) = 0, \quad (\text{A3})$$

$$g_m(r_i) = g_m(r_o) = Dg_m(r_i) = Dg_m(r_o) = 0, \quad (\text{A4})$$

where D stands for the radial differentiation operator d/dr .

The trial basis for axisymmetric fields ($n=0$) is given by

$$\mathbf{v}_m^{(1)}(r) = \begin{pmatrix} 0 \\ h_m \\ 0 \end{pmatrix}, \quad \mathbf{v}_m^{(2)}(r) = \begin{pmatrix} -ilk_0 r g_m \\ 0 \\ D(r g_m) + g_m \end{pmatrix}, \quad (\text{A5})$$

except that the third component of $\mathbf{v}_m^{(2)}$ is replaced by h_m when $l=0$, whereas for the nonaxisymmetric case the basis is

$$\mathbf{v}_m^{(1)}(r) = \begin{pmatrix} -i n g_m \\ D(r g_m) \\ 0 \end{pmatrix}, \quad \mathbf{v}_m^{(2)}(r) = \begin{pmatrix} 0 \\ -i l k_0 r h_m \\ i n h_m \end{pmatrix}, \quad (\text{A6})$$

except that the third component of $\mathbf{v}_m^{(2)}$ is replaced by h_m when $l=0$. For the projection space, the basis corresponding to axisymmetric fields is

$$\tilde{\mathbf{v}}_m^{(1)}(r) = w(x) \begin{pmatrix} 0 \\ r h_m \\ 0 \end{pmatrix}, \quad (\text{A7})$$

$$\tilde{\mathbf{v}}_m^{(2)}(r) = \frac{w(x)}{r^2} \begin{pmatrix} i l k_0 g_m \\ 0 \\ D_+ g_m + \frac{2}{r}(1 - x^2 + r x) h_m \end{pmatrix}, \quad (\text{A8})$$

where $D_+ = D + 1/r$, and the third component of $\tilde{\mathbf{v}}_m^{(2)}$ is replaced by $r h_m$ if $l=0$. The basis for the nonaxisymmetric case is

$$\tilde{\mathbf{v}}_m^{(1)}(r) = w(x) \begin{pmatrix} i n r g_m \\ r D_+(r g_m) + 2 x r^2 h_m \\ 0 \end{pmatrix}, \quad (\text{A9})$$

$$\tilde{\mathbf{v}}_m^{(2)}(r) = w(x) \begin{pmatrix} 0 \\ i l k_0 r^2 h_m \\ -i n r h_m \end{pmatrix}. \quad (\text{A10})$$

APPENDIX B: NORMAL FORM OF THE DOUBLE HOPF BIFURCATION WITH $SO(2) \times SO(2)$ SYMMETRY

The technique of Iooss and Adelmeyer,²⁴ which provides a clear and simple method to obtain normal forms, incorporating symmetry considerations, is now used for the double Hopf bifurcation with the $\mathcal{G}=SO(2) \times SO(2)$ symmetry group. In the codimension-1 Hopf bifurcation, the presence of $SO(2) \times SO(2)$ symmetry does not alter the generic normal form, and the same is true for the double Hopf bifurcation without resonance. However, it is important to specify what the resonance conditions are, because as we shall see, $SO(2) \times SO(2)$ inhibits resonance. Resonance is only possible if both the temporal frequencies (imaginary parts of the eigenvalues at the bifurcation point, ω_1^0 and ω_2^0) and the spatial frequencies (azimuthal wavenumbers, n_1 and n_2 , and axial wavenumbers, k_1 and k_2 , at the bifurcation point) satisfy the resonance condition $\omega_2^0/\omega_1^0 = n_2/n_1 = k_2/k_1 = p/q$, where p and q are positive irreducible integers. We will follow closely the analysis of the double Hopf bifurcation with $SO(2)$ and with $SO(2) \times Z_2$ symmetries provided in former related works.^{20,21}

The normal form theorem says that the dynamical system in a neighborhood of the fixed point (steady, axisymmetric basic state) in the center manifold can be cast in the form

$$\dot{z}_i = i\omega_i^0 z_i + S_i(z_1, z_2, \bar{z}_1, \bar{z}_2, \mu), \quad (\text{B1})$$

plus a complex conjugate, for $i=1, 2$. z_i are the amplitudes of the eigenvectors that bifurcate simultaneously, and μ are parameters. The functions S_i are second order in z for $\mu=0$ and satisfy

$$S(e^{iL_o^*} z) = e^{iL_o^*} S(z), \quad (\text{B2})$$

$$S(R_\alpha z) = R_\alpha S(z), \quad (\text{B3})$$

$$S(T_a z) = T_a S(z), \quad (\text{B4})$$

where L_o is the linear part of the dynamical system at criticality and L_o^* is the corresponding adjoint operator. We have used vector notation $z=(z_1, z_2, \bar{z}_1, \bar{z}_2)$ and $S=(S_1, S_2, \bar{S}_1, \bar{S}_2)$ in order to keep the expressions compact. In this notation the matrices $e^{iL_o^*}$, R_α and T_a are diagonal:

$$e^{iL_o^*} = \text{diag}(e^{-i\omega_1^0 t}, e^{-i\omega_2^0 t}, e^{i\omega_1^0 t}, e^{i\omega_2^0 t}), \quad (\text{B5})$$

$$R_\alpha = \text{diag}(e^{in_1\alpha}, e^{in_2\alpha}, e^{-in_1\alpha}, e^{-in_2\alpha}), \quad (\text{B6})$$

$$T_a = \text{diag}(e^{ik_1 a}, e^{ik_2 a}, e^{-ik_1 a}, e^{-ik_2 a}), \quad (\text{B7})$$

Equation (B2) gives the simplest form of S attainable using the structure of the linear part L_o , and Eqs. (B3) and (B4) give the additional constraints on S imposed by the symmetry group $SO(2) \times SO(2)$.

Let $z_1^{j_1} z_2^{j_2} \bar{z}_1^{l_1} \bar{z}_2^{l_2}$ be an admissible monomial in S_1 ; it must satisfy Eqs. (B2)–(B4), i.e.,

$$(j_1 - l_1 - 1)\omega_1^0 + (j_2 - l_2)\omega_2^0 = 0, \quad (\text{B8})$$

$$(j_1 - l_1 - 1)n_1 + (j_2 - l_2)n_2 = 0, \quad (\text{B9})$$

$$(j_1 - l_1 - 1)k_1 + (j_2 - l_2)k_2 = 0. \quad (\text{B10})$$

This system always admits the trivial solution $j_1 - l_1 - 1 = j_2 - l_2 = 0$. If there are no other solutions, we are in the nonresonant case; the normal form is not modified by the presence of the symmetry group $SO(2) \times SO(2)$. The nonresonant normal form is

$$S_1 = z_1 Q_1, \quad S_2 = z_2 Q_2, \quad (\text{B11})$$

where $Q_i(|z_1|^2, |z_2|^2)$, which coincides with the generic case analyzed in 22.

In order that Eqs. (B8)–(B10) have nonzero solutions, the resonant case, the condition

$$\frac{\omega_2^0}{\omega_1^0} = \frac{n_2}{n_1} = \frac{k_2}{k_1} \quad (\text{B12})$$

must be satisfied. The extra solutions are of the form

$$j_1 - l_1 - 1 = jp, \quad j_2 - l_2 = -jq, \quad j \in \mathbb{Z}, \quad (\text{B13})$$

where p/q is the irreducible form of the fraction n_2/n_1 . Additional monomials $z_1(z_1^p \bar{z}_2^q)^j |z_1|^{2l_1} |z_2|^{2l_2}$, $j \in \mathbb{Z}$, appear in the normal form. As k_1 and k_2 are positive, p and q are also positive, and we obtain

$$S_1 = z_1 Q_{11} + \bar{z}_1^{p-1} z_2^q Q_{12}, \quad (\text{B14})$$

$$S_2 = z_2 Q_{21} + z_1^p \bar{z}_2^{q-1} Q_{22}, \quad (\text{B15})$$

where $Q_{ii}(|z_1|^2, |z_2|^2, z_1^p \bar{z}_2^q)$ and $Q_{ij}(|z_1|^2, |z_2|^2, \bar{z}_1^p z_2^q)$, $i \neq j$. This is in accordance with Theorem 4.2 in Ref. 25.

Resonance in the presence of the $SO(2) \times SO(2)$ symmetry group is only possible if the resonance condition (B12) is satisfied. The spatial (both azimuthal and axial) and temporal modes must satisfy the *same* resonance condition. Notice that this condition can *never* be satisfied if the two rotating waves do not precess in the same direction, or do not propagate in the same axial direction. When these simultaneous resonance conditions are satisfied, the normal form is given by (B14) and (B15).

Substituting (B11) into (B1), we obtain the normal form in the nonresonant case:

$$\dot{z}_i = z_i [i\omega_i^0 + Q_i(|z_1|^2, |z_2|^2)]. \quad (\text{B16})$$

In terms of the moduli and phases of z_i , $z_i = r_i e^{i\phi_i}$, we have

$$\dot{r}_i = r_i Q_i^R(r_1^2, r_2^2), \quad (\text{B17})$$

$$\dot{\phi}_i = \omega_i^0 + Q_i^I(r_1^2, r_2^2), \quad (\text{B18})$$

where Q_i^R and Q_i^I are the real and imaginary parts of Q_i , respectively. Up to fourth order in r_1 and r_2 , and assuming that the coefficients of second order in Q_i^R are nonzero, the normal form can be written as²²

$$\begin{aligned}
\dot{r}_1 &= r_1(\mu_1 + p_{11}r_1^2 + p_{12}r_2^2 + q_1r_1^4), \\
\dot{r}_2 &= r_2(\mu_2 + p_{21}r_1^2 + p_{22}r_2^2 + q_2r_1^4), \\
\dot{\phi}_1 &= \omega_1^0 + \psi_1(r_1, r_2, \mu_1, \mu_2), \\
\dot{\phi}_2 &= \omega_2^0 + \psi_2(r_1, r_2, \mu_1, \mu_2),
\end{aligned} \tag{B19}$$

where we have introduced explicitly the normalized bifurcation parameters μ_1 and μ_2 . The dynamics of the moduli r_1 and r_2 decouple from the phase dynamics, and we end up with an effective two-dimensional normal form for r_1 and r_2 .

This effective normal form has four fixed points that after introducing the phase dependence, become one fixed point, two periodic solutions, and a quasiperiodic solution. The stability and regions of the existence of these solutions depend on the values of p_{ij} and q_i . There are 11 different scenarios classified in 2 categories: *simple* ($p_{11}p_{22} > 0$) and *difficult* ($p_{11}p_{22} < 0$). For a specific problem, in order to determine the corresponding scenario, there are two options. One option is to compute the normal form coefficients p_{ij} and q_i using the eigenvectors at the bifurcation point, which is very complicated in the present case. The other option is to numerically compute a regime diagram in parameter space, delineating the regions of existence of the solutions, and determine their stability in a neighborhood of the double Hopf bifurcation point, and use this information to determine the corresponding scenario; this is the approach we have employed here. Figure 6 is the regime diagram we have obtained, by computing several solutions for different parameter values close to the double Hopf bifurcation point, and computing the Hopf curves using linear stability analysis. There is only one double Hopf scenario compatible with our results, and it is the type IV of the simple case.²² We describe this scenario in detail in Sec. III.

For the simple cases ($p_{11}p_{22} > 0$), the fourth order terms in (B19) can be neglected. Introducing new variables, $\xi_1 = -p_{11}r_1^2$ and $\xi_2 = -p_{22}r_2^2$, we obtain

$$\begin{aligned}
\dot{\xi}_1 &= 2\xi_1(\mu_1 - \xi_1 - \theta\xi_2), \\
\dot{\xi}_2 &= 2\xi_2(\mu_2 - \delta\xi_1 - \xi_2),
\end{aligned} \tag{B20}$$

where $\theta = p_{12}/p_{22}$ and $\delta = p_{21}/p_{11}$. In our problem, $\theta < 0$, $\delta < 0$, and $\theta\delta < 1$. This normal form admits up to four fixed points:

$$P_0 = (0, 0), \quad P_1 = (\mu_1, 0), \quad P_2 = (0, \mu_2), \tag{B21}$$

$$P_3 = \left(\frac{\mu_1 - \theta\mu_2}{1 - \theta\delta}, \frac{\mu_2 - \delta\mu_1}{1 - \theta\delta} \right). \tag{B22}$$

P_0 exists for all values of μ_1 and μ_2 , and is stable for $\mu_1, \mu_2 < 0$. This corresponds to our basic state. P_1 exists for $\mu_1 > 0$ and is stable for $\mu_2 < \delta\mu_1$ (below the N_1 curve in Fig. 1, region 6); P_2 exists for $\mu_2 > 0$ and is stable for $\mu_2 < \theta^{-1}\mu_1$ (below the N_2 curve in Fig. 1, region 2). By including the phase information, P_1 and P_2 are limit cycles corresponding to spiral waves. P_3 exists and is stable between N_1 and N_2 (regions 3, 4, and 5 in Fig. 1). As both moduli are

nonzero for P_3 , by including the phase information, it is recognized as a quasiperiodic solution on a two-torus, and in our case it corresponds to interpenetrating spirals. For P_1, P_2 , and P_3 , r_1 and r_2 are constant, and so they have constant angular frequencies:

$$\omega_1 = \dot{\phi}_1 = \omega_1^0 + \psi_1(r_1, r_2, \mu_1, \mu_2), \tag{B23}$$

$$\omega_2 = \dot{\phi}_2 = \omega_2^0 + \psi_2(r_1, r_2, \mu_1, \mu_2).$$

In the nonresonant case, we have seen that the normal form is unaltered by the symmetry group \mathcal{G} . Nevertheless, the symmetries act on the bifurcating solutions in a well-determined fashion. From (B6) and (B7), we see that the action of \mathcal{G} leaves the moduli (r_1, r_2) invariant, and \mathcal{G} acts only on the phases (ϕ_1, ϕ_2) . The action of \mathcal{G} on the phases is

$$R_\alpha \begin{pmatrix} \phi_1 \\ \phi_2 \end{pmatrix} = \begin{pmatrix} \phi_1 + n_1\alpha \\ \phi_2 + n_2\alpha \end{pmatrix}, \tag{B24}$$

$$T_a \begin{pmatrix} \phi_1 \\ \phi_2 \end{pmatrix} = \begin{pmatrix} \phi_1 + k_1a \\ \phi_2 + k_2a \end{pmatrix}. \tag{B25}$$

The basic state P_0 is a steady solution, $r_1 = r_2 = 0$, there are no phases, and hence it is \mathcal{G} invariant. The solution P_1 has $r_2 = 0$, and so we only need to consider ϕ_1 ; as k_1 and n_1 are different from zero, both symmetries are broken. The actions of R_α and T_a are equivalent to appropriate time translations τ_α and τ_a :

$$R_\alpha: \omega_1\tau_\alpha = n_1\alpha \Rightarrow \tau_\alpha = n_1\alpha/\omega_1, \tag{B26}$$

$$T_a: \omega_1\tau_a = k_1a \Rightarrow \tau_a = k_1a/\omega_1; \tag{B27}$$

R_α and T_a become spatiotemporal symmetries; time evolution is equivalent to a rotation around the axis and also to a translation along the axis. The limit cycle can be viewed simultaneously as a rotating wave (with precession frequency $\omega_p = -\omega_1/n_1$) and also as a traveling wave in the axial direction (with axial speed $c = -\omega_1/k_1$). In fact, P_1 retains a helical symmetry: $H'_\alpha = R_\alpha T_{-n_1\alpha/k_1}$ leaves P_1 invariant; these helical symmetries generate a $SO(2)_H$ symmetry group, which is a subgroup of \mathcal{G} . The periodic solution P_1 is pointwise $SO(2)_H$ invariant, and as a set it is \mathcal{G} invariant. For this reason we call this solution a spiral wave.

The solution P_2 has $r_1 = 0$, and so we only need to consider ϕ_2 ; exactly the same considerations as for P_1 show that P_2 is a rotating wave/traveling wave with helical symmetry $SO(2)$, i.e., a spiral wave; but the helical symmetries that keep P_2 invariant are different from the ones that leave P_1 invariant. P_2 is invariant to $H'_\alpha = R_\alpha T_{-n_2\alpha/k_2}$. The helical symmetries for P_1 and P_2 are the same only when there is *spatial resonance*: $n_2/n_1 = k_2/k_1$.

The time evolution of a P_3 solution is given by

$$\Phi_t \begin{pmatrix} \phi_1 \\ \phi_2 \end{pmatrix} = \begin{pmatrix} \phi_1 + \omega_1 t \\ \phi_2 + \omega_2 t \end{pmatrix}, \tag{B28}$$

where Φ_t is the time evolution operator acting on the phases

ϕ_1 and ϕ_2 . If ω_2/ω_1 is rational, P_3 is a periodic solution; it is the *temporal resonance* case. If not, it is a quasiperiodic solution. From P_3 , the action of \mathcal{G} generates a two-torus (in the nonresonant case, where (B12) is not satisfied). The two-torus as a set is \mathcal{G} invariant, but the individual P_3 solutions do not retain any pointwise spatial symmetry (except in the case of spatial resonance). Although P_3 is quasiperiodic, in an appropriate rotating (or traveling axially) frame of reference, it becomes a periodic solution; using (B24), in an arbitrary reference frame rotating with angular velocity ω_r , the time evolution of P_3 is given by

$$R_{-\omega_r t} \Phi_t \begin{pmatrix} \phi_1 \\ \phi_2 \end{pmatrix} = \begin{pmatrix} \phi_1 + (\omega_1 - n_1 \omega_r) t \\ \phi_2 + (\omega_2 - n_2 \omega_r) t \end{pmatrix}. \quad (\text{B29})$$

When ω_r is such that $(\omega_1 - n_1 \omega_r)/(\omega_2 - n_2 \omega_r)$ is rational, P_3 is *periodic* in the rotating reference frame. The two simplest choices are $\omega_r = \omega_i/n_i$, for $i=1$ and 2 . These choices are precisely the precession frequencies of the pure modes P_1 and P_2 .

- ¹D. D. Joseph, *Stability of Fluid Motions I and II*, No. 27 in Springer Tracts in Natural Philosophy (Springer-Verlag, Berlin, 1976).
- ²H. A. Snyder, "Experiments on the stability of spiral flow at low axial Reynolds numbers," Proc. R. Soc. London, Ser. A **265**, 198 (1962).
- ³D. I. Takeuchi and D. F. Jankowski, "A numerical and experimental investigation of the stability of spiral Poiseuille flow," J. Fluid Mech. **102**, 101 (1981).
- ⁴H. M. Nagib, "On instabilities and secondary motions in swirling flows through annuli," Technical Report, Illinois Institute of Technology, 1972.
- ⁵R. M. Lueptow, A. Docter, and K. Min, "Stability of axial flow in an annulus with a rotating inner cylinder," Phys. Fluids A **4**, 2446 (1992).
- ⁶A. Tsameret and V. Steinberg, "Competing states in a Couette-Taylor system with an axial flow," Phys. Rev. E **49**, 4077 (1994).
- ⁷S. T. Wereley and R. M. Lueptow, "Velocity field for Taylor-Couette flow with an axial flow," Phys. Fluids **11**, 3637 (1999).
- ⁸A. Pinter, M. Lücke, and C. Hoffmann, "Spiral and Taylor vortex fronts and pulses in axial through flow," Phys. Rev. E **67**, 026318 (2003).
- ⁹M. Langenberg, M. Heise, G. Pfister, and J. Abshagen, "Convective and

- absolute instabilities in counter-rotating spiral Poiseuille flow," Theor. Comput. Fluid Dyn. **18**, 97 (2004).
- ¹⁰C. Hoffmann, M. Lücke, and A. Pinter, "Spiral vortices and Taylor vortices in the annulus between rotating cylinders and the effect of an axial flow," Phys. Rev. E **69**, 056309 (2004).
- ¹¹K. C. Chung and K. N. Astill, "Hydrodynamic instability of viscous flow between rotating coaxial cylinders with fully developed axial flow," J. Fluid Mech. **81**, 641 (1977).
- ¹²M. A. Hasoon and B. W. Martin, "The stability of viscous axial flow in an annulus with a rotating inner cylinder," Proc. R. Soc. London, Ser. A **352**, 351 (1977).
- ¹³D. L. Cotrell and A. J. Pearlstein, "The connection between centrifugal instability and Tollmien Schlichting-like instability for spiral Poiseuille flow," J. Fluid Mech. **509**, 331 (2004).
- ¹⁴A. Meseguer and F. Marques, "On the competition between centrifugal and shear instability in spiral Poiseuille flow," J. Fluid Mech. **455**, 129 (2002).
- ¹⁵A. Meseguer and F. Marques, "On the stability of medium gap co-rotating spiral Poiseuille flow," Phys. Fluids **17**, 094104 (2005).
- ¹⁶C. Canuto, M. Y. Hussaini, A. Quarteroni, and T. A. Zang, *Spectral Methods in Fluid Dynamics* (Springer-Verlag, New York, 1988).
- ¹⁷A. Meseguer, "Streak breakdown instability in pipe Poiseuille flow," Phys. Fluids **15**, 1203 (2003).
- ¹⁸A. Meseguer and L. Trefethen, "Linearized pipe flow to Reynolds number 10^7 ," J. Comput. Phys. **186**, 178 (2003).
- ¹⁹R. D. Moser, P. Moin, and A. Leonard, "A spectral numerical method for the Navier-Stokes equations with applications to Taylor-Couette flow," J. Comput. Phys. **52**, 524 (1983).
- ²⁰F. Marques, J. M. Lopez, and J. Shen, "Mode interactions in an enclosed swirling flow: a double Hopf bifurcation between azimuthal wavenumbers 0 and 2," J. Fluid Mech. **455**, 263 (2002).
- ²¹J. M. Lopez and F. Marques, "Mode competition between rotating waves in a swirling flow with reflection symmetry," J. Fluid Mech. **507**, 265 (2004).
- ²²Y. A. Kuznetsov, *Elements of Applied Bifurcation Theory*, 3rd ed. (Springer-Verlag, New York, 2004).
- ²³A. Meseguer and F. Marques, "Bicritical instabilities in pressure driven helicoidal flows," J. Phys.: Conf. Ser. **14**, 228 (2005).
- ²⁴G. Iooss and M. Adelmeyer, *Topics in Bifurcation Theory and Applications*, 2nd ed. (World Scientific, Singapore, 1998).
- ²⁵M. Golubitsky, I. Stewart, and D. G. Schaeffer, *Singularities and Groups in Bifurcation Theory. Volume II*, Vol. 69 of Applied Mathematical Sciences (Springer-Verlag, New York, 1988).